The Wave Origins of Longitudinal Structures in ExoMars Trace Gas Orbiter (TGO) Aerobraking Densities

Jeffrey M. Forbes, Sean Bruinsma, Xiaoli Zhang, Francois Forget,
Jean-Charles Marty, Ehouarn Millour, Francisco González-Galindo

The Wave Origins of Longitudinal Structures in ExoMars Trace Gas Orbiter (TGO) Aerobraking Densities

Jeffrey M. Forbes[1] , **Sean Bruinsma[2]** , **Xiaoli Zhang[1]** , **Francois Forget[3]**, **Jean-Charles Marty[2]**, **Ehouarn Millour[3]** , and **Francisco González-Galindo[4]**

[1]Ann and H.J. Smead Department of Aerospace Engineering Sciences, University of Colorado, Boulder, CO, USA, [2]Space Geodesy Office, CNES, Toulouse, France, [3]Laboratoire de Mètèrologie Dynamique, CNRS, Paris, France, [4]Instituto de Astrofísica de Andalucía, CSIC, Granada, Spain

Abstract The nature and origins of longitudinal density structures in Mars' thermosphere between 100 and 120 km altitude, and −30° and −75° latitude around winter solstice (Ls = 70–122°), as measured by the accelerometer on the ExoMars Trace Gas Orbiter (TGO) Mission, are investigated. The methodology consists of deducing the responsible waves by comparing the observed longitude versus local time phase progressions of the structures with those of probable candidate waves in the Mars Climate Database (MCD) climatology. The observed wave-1, wave-2, and wave-3 structures are interpreted as originating mainly from SPW1; (SPW2, S0, DE1); and (SPW3, DE2), respectively, where SPWm denotes a stationary planetary wave with zonal wavenumber $s = m$, S0 is the zonally symmetric semidiurnal tide, and DE1(DE2) are the eastward-propagating diurnal tides with $s = -1(-2)$. All of these waves exist in the MCD with amplitudes as large as those observed, although not wholly in the narrow height-latitude regime accessed by TGO. This disparity between the MCD and TGO amplitude structures is hypothesized to result from the extreme intrusion of the polar-region eastward winter jet into the thermosphere in the MCD. The winter polar jet blocks poleward expansion of DE1 and DE2 beyond −30° latitude, and also impacts the structures of SPW2, S0 and SPW3 that arise from in situ nonlinear interaction between DE1 and DE2, respectively, with the diurnal migrating tide (DW1).

1. Introduction

Total mass density measurements from accelerometers on Mars Global Surveyor (MGS) in 1997–1998, Mars Odyssey (MO) in 2001, and Mars Reconnaissance Orbiter (MRO) in 2006 have served as sources of information on the structure and variability of Mars' mesopause-lower thermosphere (MLT) region (ca. 90–130 km). Inserted into orbit on December 25, 2003, the SPICAM instrument on Mars Express provided a decade's worth of complementary stellar occultation measurements of temperature between 50 and 150 km that included defining the location and variability of the mesopause (Forget et al., 2009; Montmessin et al., 2017), which lies between 100 and 120 km depending on latitude and season. The accelerometer measurements have provided information on longitude variability, which has generally been attributed to solar-asynchronous tides which are mainly manifested as wave-1, wave-2, wave-3, and wave-4 longitudinal structures as measured from the quasi-Sun-synchronous orbits of MGS, MO, and MRO (e.g., Angelats i Coll et al., 2004; Forbes & Hagan, 2000; Joshi et al., 2000; Moudden & Forbes, 2015; Wang et al., 2006; Wilson, 2002; Withers, 2006; Withers et al., 2003). Similar longitude structures and tidal interpretations apply to neutral mass spectrometer (e.g., England et al., 2016; Liu et al., 2017) and ultraviolet imager (e.g., England et al., 2016; Lo et al., 2015) measurements at somewhat higher altitudes (~170–200 km) on the Mars Atmosphere and Volatile Evolution (MAVEN) mission. However, except for a few isolated cases where local solar time (LST) changed sufficiently fast over restricted ranges of latitude and Ls (e.g., England et al., 2019; Forbes et al., 2004; Forbes & Zhang, 2018), the lack of local time coverage has generally impeded definitive identification of the specific solar tides contributing to the longitudinal structures.

In this paper, densities between 102 and 120 km inferred from accelerometer measurements during aerobraking operations as part of the ExoMars Trace Gas Orbiter (TGO) Mission, are analyzed with focus on the nature and origins of longitudinal variability in density. Since the TGO orbit migrates in local time, new insights into the wave origins of the density structures are enabled, particularly around the S. Hemisphere polar region during the winter season. The interpretation is aided by the Mars Climate Database (MCD

Version 5.3; Millour et al., 2018) derived from numerical simulations of the LMD Mars Global Climate Model (Forget et al., 1999). The MCD provides climatological density variations due to tides and stationary planetary waves under the same Mars conditions that are sampled by the TGO accelerometer. Suitability of the MCD climatology for this type of work is provided by Forbes et al. (2020), who demonstrate consistency of MCD tidal temperatures with those inferred from MRO Mars Climate Sounder (MCS) measurements at 76 km (Kleinböhl et al., 2009), and with accelerometer-measured densities between 105 and 115 km during Phase II aerobraking of MGS, which covered Ls = 36–92°. On the other hand, the MCD has not been extensively tested against thermosphere density data, and the TGO measurements provide a new opportunity to evaluate the MCD, and perhaps to guide its future development.

The following section describes the MCD and how it is utilized to aid interpretation; how densities are derived from TGO accelerometer measurements, and estimated uncertainties; how the density data are processed prior to scientific analysis; and how tides are inferred from local time variations of longitudinal wave components. Section 3 presents the results, and section 4 is reserved for a brief summary and conclusions.

2. Methodology

2.1. The MCD Model

The Mars Climate Database (MCD) provides meteorological fields that are derived from a surface to exosphere (∼300 km) Mars general circulation model (MGCM) developed at the Laboratoire de Météorologie Dynamique (http://www-mars.lmd.jussieu.fr). The LMD-MGCM originated in the early work of Forget et al. (1999), and since then has been extended into the thermosphere and ionosphere (Gonzalez-Galindo et al., 2009, 2013, 2015), and more sophisticated and realistic treatments of dust and water cycles, photochemistry, radiative transfer, and solar radiative fluxes have been introduced. The MCD climatological database is organized according to climatologies representing several lower-atmosphere dust and solar activity levels. In this study, we use the climatology scenario from MCD Version 5.3 (Millour et al., 2018), in which dust distributions are based on those observed in Mars years when no global dust storms occurred, and solar minimum EUV conditions are assumed (i.e., E10.7 = 80, roughly consistent with actual solar conditions during TGO aerobraking). The MCD dust climatology during TGO aerobraking in fact closely approximates the atmospheric dust content for MY34, Ls ∼30–130 (Montabone et al., 2020).

The climatological database consists of data files containing meteorological output for a mean day (with 12 values per day, or every 2 h) per Martian month (i.e., Ls values of 0–30°, 30–60°, 60–90°, …). In order to sample the MCD at the height, latitude, longitude, time, and Ls of each TGO measurement (see section 3), the MCD-supplied software is utilized, which applies linear interpolation in space, time of day and month to the data files stored in the MCD. Altitudes above the Mars areoid are utilized here for both the MCD and TGO data. Note that the emphasis here is on utilizing the MCD to assist in assessing the plausibility of our TGO tidal interpretations, and not on interpreting, e.g., intraseasonal variability that would require utilization of the LMD GCM simulations that form the basis of the MCD.

2.2. TGO Accelerometer Measurements and Density Product

The data employed in this study are thermosphere total mass densities inferred from accelerometer measurements on Exomars TGO when it was in the aerobraking phase of its mission (Siddle et al., 2020), from March 14, 2017 to February 20, 2018. The High Gain Antenna (HGA) was pointed toward Earth and the solar arrays were facing the Sun in the nominal mode of the orbit. To protect TGO against the large heat flux encountered at the lowest altitudes it was rotated into aerobraking mode every orbit upon approaching periapsis. In that mode, the thruster faced the flight direction, the solar arrays were rotated to be nearly perpendicular to the velocity vector in order to maximize the drag effect, and the HGA was stowed.

Over the aerobraking phase of less than one Earth year, the apoapsis altitude of 34,000 km was reduced to 1,000 km. Over that same period, the orbital period decreased from 24 to 2 h, while the number of orbits per day increased from one to 11. In this study, data from before the solar conjunction (during which aerobraking was suspended) in the summer of 2017 is not used. The aerobraking resumed on September 8, 2017, with two aerobraking passes per day and an orbital period of almost 14 h.

TGO's inertial measurement package contains low-resolution engineering accelerometers, which are used to measure the large accelerations during maneuvers. During the aerobraking phase the spacecraft dipped down to very low altitudes and atmospheric drag accelerations could be measured with good signal to noise ratios close to periapsis. The calibrated 1 Hz accelerations were used to compute atmospheric densities ρ along TGO's trajectory up to a maximum altitude of 150 km by scaling the model densities as follows:

$$\rho^{\text{TGO}} = \frac{a_{-x}^{\text{TGO}}}{a_{-x}^{\text{dragmodel}}} \cdot \rho_{\text{model}} \tag{1}$$

where the numerator corresponds to the $-x$ component of the measured accelerations, which is approximately in the direction of the satellite velocity, and the denominator to the projection of the modeled drag acceleration on the same axis. Solar radiation pressure is negligible below 150 km altitude compared with atmospheric drag, and, in the absence of thrusts and after removal of angular accelerations, the measured acceleration is due to atmospheric drag. The drag force acting on TGO is modeled with a box-and-wings model, using flat plates (six for the bus and two for the two solar arrays) with areas, optical properties and mass provided by the European Space Operations Center (ESOC). This simplified satellite shape model is oriented in inertial space to compute the satellite ram area perpendicular to the velocity with respect to the atmosphere using the telemetered quaternions with negligible error. The drag acceleration is modeled as follows:

$$a_{\text{drag}} = \frac{1}{2} C_D \frac{\text{TGO(ramarea)}}{\text{TGO(mass)}} \rho_{\text{model}} v^2 \tag{2}$$

with the drag coefficient C_D, and v the spacecraft velocity with respect to the atmosphere. Mars-GRAM 2005 (Justh & Justus, 2007) was used to compute the model densities. The drag coefficient, modeled under the assumptions of hyperthermal free-molecular flow and diffuse re-emission of the particles according to Sentman (1961) with complete accommodation, is 2.20. This value is very close to what Tolson et al. (2005) used for Mars Odyssey at similar periapsis altitudes.

The uncertainty in the derived density is the sum of a systematic part due to the uncertainty in C_D, estimated to be 5% at these very low altitudes, and an instrumental noise and bias due to the accelerometer. The systematic error has no impact on analyses of relative variations such as due to wave-like perturbations. The noise on the TGO accelerations is estimated at 0.0005 m s^{-2} by Siddle et al. (2020). The maximum exploitable altitude of the density profiles is about 120 km taking the Signal to Noise Ratio (SNR) into account. The SNR and average SNR as a function of altitude, and as a function of altitude over the study period, are presented in Figures S1 and S2 in the supporting information. The average SNR is always better than 10 at periapsis, whereas at 120 km the average drops to about 2.5 with excursions smaller than one at the end of the aerobraking phase. Additional smoothing is performed as part of the data processing (see below), which further reduces noise.

2.3. Data Processing

The TGO density data examined in this study include 511 orbit segments below 120 km around the time of periapsis, extend from September 8, 2017 to February 21, 2018 (Ls = 58° to Ls = 133°), and are smoothed with a 40-s moving window to remove small-scale variability. Figures 1a–1c illustrate how periapsis latitude and local solar time (LST) (solar true local time, as in the MCD), longitude, and height change with Ls, respectively. Longitudinal coverage is poor for Ls < 68° and Ls > 128° (see Figure 1b), so these periods are omitted from analysis. Data from two orbits within the remaining range of Ls that deviated unrealistically from adjacent orbits were considered outliers and rejected. Data points in each orbit segment in the 111–113 km range are averaged into one point (hereafter "112 km"), and so are those in the 118–120 km altitude range (hereafter "119" km). Three data sets are therefore formed: periapsis, 112 and 119 km, each containing 131 sols of data. Each data point of each data set is indexed according to its corresponding average latitude, longitude, LST, and altitude.

Figure 1 also delineates two different phases within the TGO data acquisition period, indicated by the yellow and pink rectangles. The first "nonpolar" (yellow) phase, extends from Ls = 70° to Ls = 106° wherein
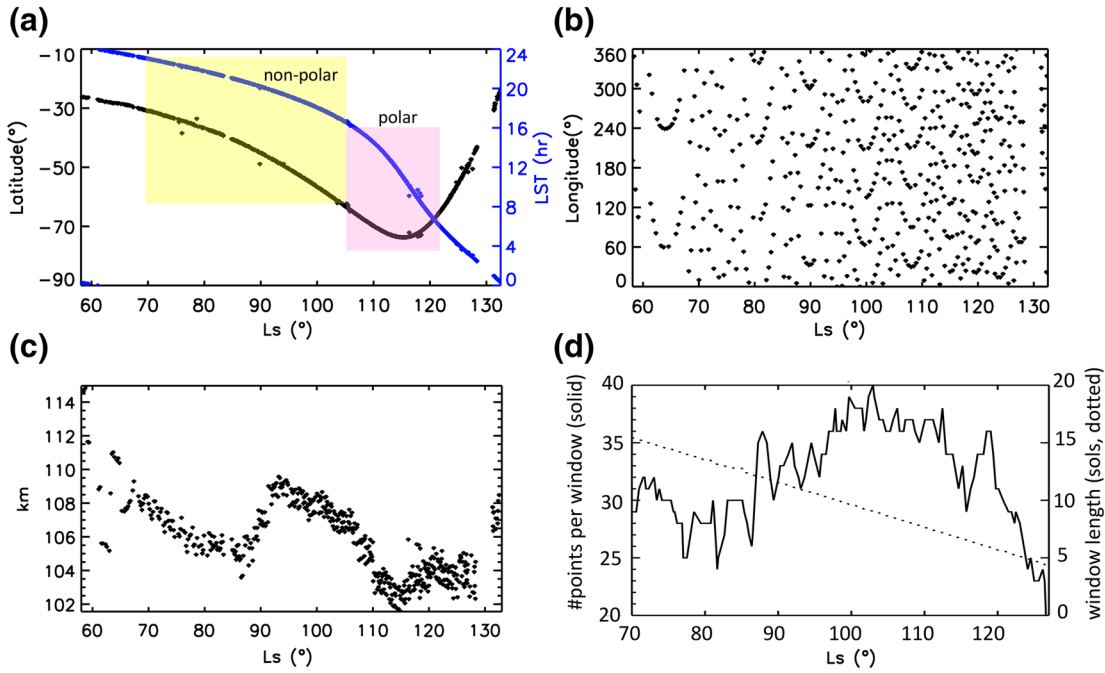
Figure 1. Orbital, sampling, and fitting information pertinent to analysis of the TGO data. (a) Periapsis latitude (black line) and LST (blue line) versus Ls. The yellow and pink rectangles encompass the latitudes and LSTs for the nonpolar and polar intervals analyzed and depicted in later figures. (b) Longitude of periapsis versus Ls. (c) Altitude of periapsis versus Ls. (d) Fitting window length (dotted line) and number of points per fitting window (solid line); the fitting window is moved one sol forward at a time. TGO, Trace Gas Orbiter; LST, local solar time.

latitude increases poleward from about −30° to −65°, and local time decreases from about 2300 LST to 1600 LST. The second "polar" (pink) phase extends from Ls = 106° to Ls = 122° wherein latitude increases from ≈−65° to ≈−75° and then back down to ≈−65°, and LST decreases from 16:00 to 06:00. Available data after Ls = 122° only extends to Ls = 128° (see above) with only a 3-h change in LST, and is not considered for subsequent analysis.

Defining and then harmonically decomposing longitudinal structures within certain segments of time requires adequate data coverage in longitude within that time segment. In keeping with the desire to leverage LST variability in the analyses of the TGO density measurements, we experimented in a trial-and-error fashion with longitudinal fitting within various time segments or "windows," with a view toward balancing the attainment of definitive longitudinal structures while minimizing the range of local times and/or latitudes that are included within the fit. From Ls = 68° to Ls = 128°, the number of data points of each sol increases with time, due to contraction of the TGO orbit and decrease in its orbital period compared to Mars' rotation period, which determines the number of longitudes sampled per sol. This enabled a changing window length with time given by 16 − (Ls − 68.82°)/5 sols, as illustrated by the dotted line in Figure 1d, and consequently enabled higher time resolution after Ls ≈ 105° when LST was changing more rapidly. The data points within each fitting window were averaged into 10° longitude bins. Values in empty longitude bins were replaced with linearly interpolated values based on nearby nonempty bins. The resulting longitudinal variation within each window was then decomposed into zonal waves based on a linear least squares fit of the following function:

$$A_0 + \sum_{k=1}^{3} [a_k cos(k\lambda) + b_k sin(k\lambda)] = A_0 + \sum_{k=1}^{3} A_k cos(k(\lambda - \lambda_k)) \tag{3}$$

where A_0 is the longitude-mean density, λ is longitude, A_k is the amplitude of the kth zonal component, and λ_k is the longitude of maximum of the kth zonal component. Throughout this paper, the amplitudes A_k are expressed in percent fractions of A_0.

Longitudinal fits of the type depicted in (3) were limited to three zonal components since adding a fourth component did not change the fits to zonal structures very much, and the TGO wave-4 results were not
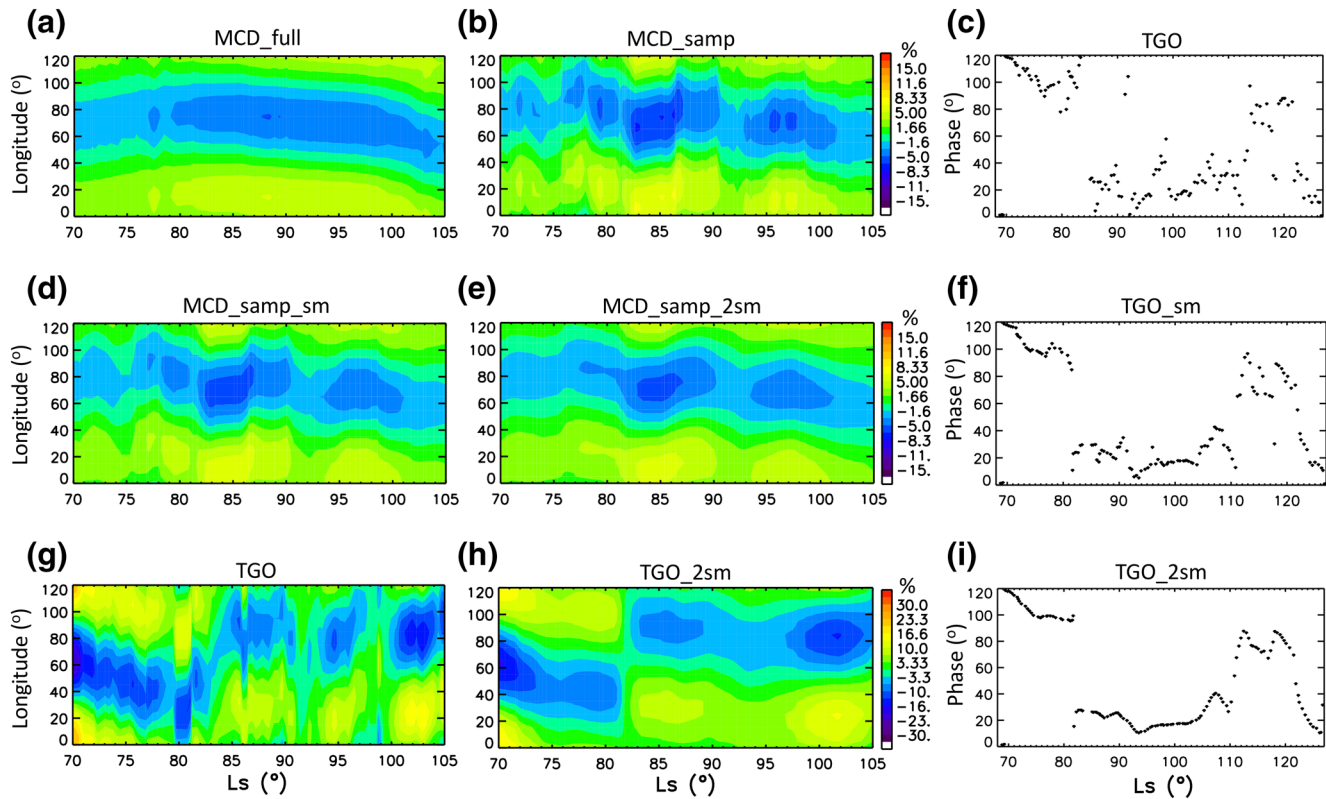
Figure 2. Sample results illustrating how TGO densities were smoothed to ameliorate variability introduced by sampling of Mars atmosphere. All panels pertain to wave-3 density structures (% relative to zonal mean) at 112 km plotted as a function of longitude (y axis) and Ls (x axis). (a), (b), (d), (e): amplitudes corresponding to MCD_{full}, MCD_{samp}, MCD_{samp_sm}, MCD_{samp_2sm}; (g), (h): amplitudes corresponding to TGO, TGO_{2sm}; (c), (f), (i) phases (longitudes of density maxima) corresponding to TGO, TGO_{sm}, TGO_{2sm}. TGO, Trace Gas Orbiter; MCD, Mars Climate Database.

as conducive to interpretation as $k = 1, 2, 3$. This is at least partially due to the fact that the longitudinal sampling affected $k = 4$ more than the other zonal components. TGO longitude sampling was in fact not synchronous with time, but rather contained periodic patterns related to contraction of the orbit. These are visible in Figure 1b, e.g., around Ls = 60–70° and Ls = 100–110°. The sampling moreover introduced a variability of its own into the derived zonal components. In addition to using the MCD output as a reference for scientific interpretation, it is also used here to gain insights into the influences of satellite sampling on the zonal harmonic decomposition of the longitudinal structures, and to explore actions to ameliorate these effects.

Figure 2, which pertains to the nonpolar 112-km altitude dataset, and zonal component $k = 3$, illustrates the sampling effects noted above. Presented here are TGO and MCD $k = 3$ density amplitudes with various degrees of smoothing to be described below, extending from Ls = 70° ($\approx -30°$) to Ls = 105° ($\approx -65°$ latitude). Figure 2a illustrates $k = 3$ density amplitudes extracted from MCD at 112 km and at the same latitudes and local times as TGO, but with complete longitude coverage (denoted MCD_{full}). Figure 2b is similarly derived, except that TGO sampling is used, and is denoted MCD_{samp}. The MCD_{samp} structures in Figure 2b compared to the MCD_{full} structures in Figure 2a isolate the influences of satellite sampling on the fits using expression (3). This effect was recently reported in Forbes et al. (2020) in the context of fitting MGS accelerometer densities, but no previous studies involving decomposition of longitudinal structures in Mars atmosphere have reported on the influences of satellite sampling.

Figure 2g illustrates the $k = 3$ density amplitudes derived from TGO. The illustrated density variability not only includes sampling effects of the type illustrated in Figure 2b, but potentially also includes variations due to latitude-Ls changes in forcing and modulation by planetary waves (see, e.g., Moudden & Forbes, 2010, 2011) which may additionally exacerbate the influences of sampling. Since our main objective in this paper is to employ relatively slow LST variations to make inferences about the underlying presence

of certain tidal components, the tactic adopted to ameliorate the influences of short-term variability is to smooth the TGO structures in time. This approach is also consistent with the climatological nature of the MCD, and its use to inform us on what tidal components might credibly produce the structures manifested in the TGO measurements.

The smoothing applied to TGO should have the effect of significantly reducing the short-term variability, but should minimally affect variability at the longer time scales associated with LST changes. To guide this endeavor, the smoothing was applied to MCD_{samp} and checked against similar plots ordered in LST (see Figures 6–8) to assess its effectiveness. As a first step, 10-Ls(5-Ls) running means were applied to the densities in each longitude bin between Ls = 70–105°(Ls = 106–122°), and expression (3) was fit to these data to obtain the MCD_{samp_sm} density structures illustrated in Figure 2d. It was decided that additional smoothing would be desirable and could be tolerated, and the $k = 3$ postfitting structures of the type in Figure 2d were subjected to the same 10-Ls(5-Ls) smoothing in time to obtain the MCD_{samp_2sm} smoothed structures in Figure 2e. The same steps were applied to the TGO densities to obtain the final end product of this effort, TGO_{2sm} in Figure 2h.

A complementary perspective on the smoothing of TGO as described above is provided in Figures 2c, 2f, and 2i, where the $k = 3$ phases are depicted for the sequence TGO, TGO_{sm}, and TGO_{2sm}. Here the illustration extends from Ls = 68° to Ls = 128°, and thus includes the nonpolar and polar phases and more. These types of plots assist in understanding the nature of phase jumps. For instance, in Figure 2i, the phase jump around Ls = 80° is determined to be real and not an artifact, and moreover might be more appropriately interpreted as −20° to +30°, instead of 100° to 30°.

All of the panels of the type illustrated in Figure 2 were replicated for $k = 1, 2, 3$; periapsis, 112 and 119 km altitude; for both polar and nonpolar phases; and with x-axes ordered in both Ls and LST. The scientific analysis reported on in section 3 compares MCD_{full} and TGO_{2sm} structures with LST as the x axis. The supporting information includes amplitude and phase plots of the type provided in Figure 2i, comparing TGO_{2sm} and MCD_{samp_2sm} within the same panels.

To get a rough idea of the density variability reflected in the model and in the TGO measurements, the mean amplitudes and their standard deviations for the MCD and TGO wave-1, wave-2, and wave-3 longitudinal density structures in the supporting information were calculated and appear in Table 1. Roughly, the MCD wave-1, wave-2, and wave-3 amplitudes are about half those of TGO. To varying degrees, the standard deviations are also smaller for the MCD, but this is not unexpected for a climatology. For both MCD and TGO, some part of the variability is due to sampling effects which were not fully removed.

2.4. Methodology for Inferring Wave Components

In this subsection a methodology is described whereby insights into the tidal components that underly the longitudinal structures can be inferred based upon how those structures evolve with respect to both longitude and local time, in the absence of sufficient local time coverage to actually derive tidal components reliably. It was first applied by Forbes et al. (2004) to the interpretation of MGS Phase-I midlatitude aerobraking densities near 125 km. After a long hiatus, it was very recently applied by Forbes et al. (2018) to Odyssey and MRO aerobraking densities at 100–120 km altitude and by England et al. (2019) to MAVEN mass spectrometer density measurements near 200 km altitude, both in Mars high-latitude regions.

To arrive at the operationally useful formula, we begin with the mathematical expression for an atmospheric tide in any atmospheric variable:

$$A_{n,s}cos(n\Omega t + s\lambda - \phi_{n,s}) \tag{4}$$

where $A_{n,s}$ is the tidal amplitude; $\Omega = 2\pi \, sol^{-1}$; $n = 1, 2, 3$ refers to 24-h (diurnal), 12-h (semidiurnal) and 8-h (terdiurnal) periods, respectively; s is the zonal wavenumber; t is time; λ is longitude; and $\phi_{n,s}$ is the phase. Note that $A_{n,s}$ and $\phi_{n,s}$ are functions of height and latitude. A solar-synchronous tide that "migrates" with the westward motion of the Sun to a ground-based observer corresponds to $s = n$ and appears the same at

all longitudes. Longitudinal variability is captured by a range of wavenumbers $s \neq n$ at each frequency. Converting (4) to the local time frame leads to:

$$A_{n,s} cos(n\Omega t_{LST} + (s - n)\lambda - \phi_{n,s}) \tag{5}$$

At a fixed LST, $k = |s - n|$ is the space-based zonal wavenumber, and corresponds to the kth zonal component in expression (3), and thus relates a tide with given s and n to a particular zonal component of a total longitudinal structure.

Setting the derivative of the quantity in brackets in (5) equal to a constant and taking the derivative relates LST and longitude for a tide with given n, s:

$$\frac{dt_{LST}}{d\lambda} = \frac{n - s}{n\Omega} = \frac{n - s}{n} \cdot \frac{4.0h}{60°} \tag{6}$$

As demonstrated below, this relationship can be used to eliminate some of the ambiguity in identifying the presence or absence of a given tidal component in the data. The $\frac{4.0h}{60°}$ factor is chosen for convenience of scale in interpreting upcoming Figures.

In this paper, we adopt the conventional notation DWs or DEs to denote a westward or eastward-propagating diurnal tide, respectively, with zonal wavenumber $= s$. For semidiurnal and terdiurnal oscillations "S" and "T," respectively, replaces "D." The zonally symmetric oscillations are denoted D0, S0, T0. In addition, stationary planetary waves ($n = 0$) with $k = 1, 2$, three are independent of time, and are denoted SPW1, SPW2, SPW3, respectively. Table 2 lists values of $dt_{LST}/d\lambda$ of the various tides and SPWs pertinent to the present study.

2.5. Wave Components in the MCD

In the previous section, the MCD was utilized to understand the influences of satellite sampling on the extraction of longitudinal structures in density, and to guide the described mitigation strategy. The final part of this methodology section describes how the MCD is utilized to support scientific interpretation of TGO longitude structures, basically to provide plausibility and credibility to the interpretations made on the basis of expression (6). At the same time this analysis provides the opportunity to identify shortcomings in the MCD tidal specifications. The recent study by Forbes et al. (2020) in fact addressed tidal coupling between the middle and upper atmosphere of Mars as represented by the MCD, with particular emphasis on the processes that influence tidal variations in total mass density between 76 and 172 km altitude as a function of Ls and latitude. The veracity of the MCD was underscored by its ability to capture the amplitudes and seasonal-latitudinal variability of MRO/MCS tidal temperatures at 76 km altitude, and longitudinal structures measured by the MGS accelerometer between 105 and 115 km and Ls = 45–85°. Forbes et al. (2020) found that the solar-asynchronous tides that contributed most to longitude variability at low and middle latitudes above 100 km altitude included DE3, DE2, DE1, S0, and SE1, in keeping with analyses of thermosphere density structures conducted in the past 2 decades by several authors and reviewed in the Introduction. Forbes and Zhang (2018) most recently analyzed accelerometer density measurements during MO and MRO aerobraking around the winter polar regions, and additionally invoked D0, SPW1, and SPW2 in the context of interpreting the observed longitude variability. The MCD and Forbes et al. (2020) reinforce these new interpretations, and clarify the presence of "Kelvin wave-like" oscillations at high latitudes (e.g., DE1), and SPW at low latitudes and high altitudes. There are also additional wave components in the MCD (e.g., SW1, SPW3) that did not rise to the importance of the aforementioned tides in Forbes et al. (2020), but which do appear in the forthcoming TGO analysis.

It is relevant to note that the MCD simulations employed in Forbes et al. (2020) corresponded to average solar EUV conditions (E10.7 at Earth = 140), whereas those used for the current study correspond to E10.7 = 80 in keeping with the solar conditions during TGO aerobraking. As it turns out, when cast as percent residuals from the zonal mean, the tidal density perturbations in the MCD at E10.7 = 80 as compared with E10.7 = 140 do not reflect any significant differences. This result could perhaps have been anticipated,
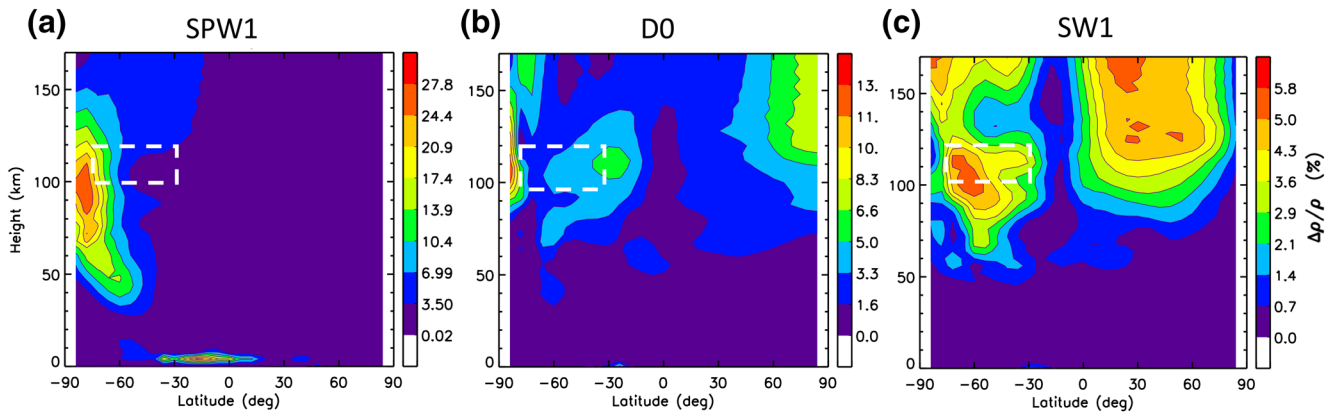
Figure 6. Wave-1 density structures (% perturbations about the zonal mean) as a function of longitude and LST for TGO (top six panels) and MCD (bottom six panels) for the nonpolar (left) and polar (right) analysis phases. Within each set of six panels for MCD or TGO, the panels are ordered top to bottom: 119 km, 112 km, and periapsis. Ls scale is provided at the top of each column. Note that all the MCD(TGO) scale ranges are ±15%(±30%). Dashed lines and corresponding labels indicate the dominant contributing wave to the longitude structure in each panel. LST, local solar time; TGO, Trace Gas Orbiter; MCD, Mars Climate Database.

but nevertheless is an important point to bear in mind when comparing and interpreting thermosphere density perturbations between different levels of solar activity.

All of the tides (DE2, DE1, D0, SW1, S0, SPW1, SPW2, SPW3) pertinent to our interpretation of TGO variability in the following section are now briefly described in Figures 3–5 in terms of their height-latitude structures and potential origins. As noted in Forbes et al. (2020; see also Angelats i Coll et al., 2004; Moudden and Forbes, 2008), some wave components in the thermosphere arise from nonlinear interactions between other wave components according to theory of Teitelbaum and Vial (1991). That is, the interaction between two primary waves yields two secondary waves, one (SW+) with frequency and zonal wavenumber corresponding to the sum of those of the interacting (primary) waves, and another (SW−) corresponding to the difference between the primary wave frequencies and zonal wavenumbers. For tides and SPW, we can use the simple notation $[n_1, s_1] \times [n_2, s_2] \rightarrow [n_2 + n_1, s_2 + s_1] + [n_2 - n_1, s_2 - s_1]$ where n_1 or n_2 correspond to 0, 1, or two for a SPW, diurnal tide, or semidiurnal tide, respectively, consistent with the notation in (4); similarly, s_1 or s_2 are the zonal wavenumbers of the primary waves. So, for example, interaction between SPW1 and SW2 can be written: $[0, +1] \times [2, +2] \rightarrow [2, +3] + [2, +1]$ where $SPW1 = [0, +1]$, $SW2 = [2, +2]$, $SW+ = SW3 = [2, +3]$, and $SW− = SW1 = [2, +1]$.

In the mathematical and modeling formulation of Teitelbaum and Vial (1991), the nonlinear interactions between primary wave variables appear mainly in advective terms in the continuity, thermal energy and momentum equations. Although figures in this paper display height-latitude structures of total mass density fields associated with various waves, the reader is reminded that the horizontal wind fields associated with these waves play a key role in the interactions leading to secondary waves, and that the wind field distributions are often quite different than those of density.

Figure 3 illustrates height-latitude structures of (a) SPW1, (b) D0, and (c) SW1, respectively, each one corresponding to a $k = |s − n| = 1$ longitudinal structure. All panels refer to the MCD climatological month Ls = 90–120°. This is representative of large portions of both nonpolar and polar phases of our analysis, and serves adequately to demonstrate the plausibility of each wave component inferred to actually exist in Mars thermosphere vis-a-vis TGO density measurements. During Ls = 60–90° in the MCD, SPW1 achieves slightly larger amplitudes and extends further equatorward and upward in altitude than shown here in Figure 3a. The existence of SPW1 is a well-known feature of Mars' winter polar middle atmosphere, and was also shown to extend well above 100 km in the GCM simulation of Moudden and Forbes (2008). D0 as shown in Figure 3b is zonally symmetric and thus can exist at the pole with nonzero values in perturbation temperature, density, pressure and vertical velocity, since continuity over the pole is not interrupted for these quantities. Waves with $s \neq 0$ generally do not exist at the pole since they violate continuity, the one exception being the horizontal wind field for $s = 1$. D0 mainly originates from the modulation of surface
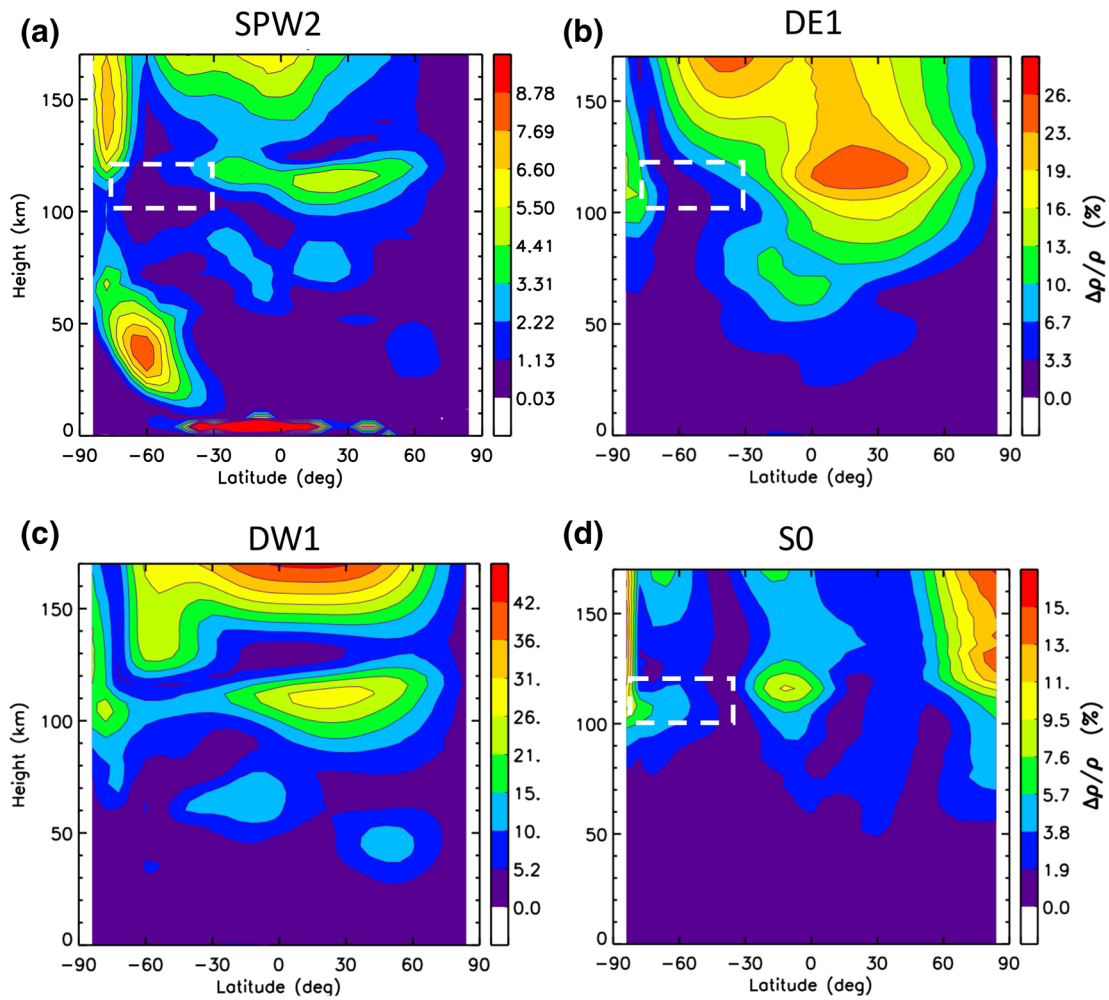
Figure 7. Same as Figure 6, except for wave-2 longitude structures in density. Note that the longitude scales only extend from 0° to 180°, since for wave-2 the structures between 180° and 360° longitude by definition duplicate those between 0° and 180°.

thermal heating by the wave-1 component of topography, with surface thermal inertia and albedo playing secondary roles, and production through several nonlinear interactions ($SPW1 \times DW1$, $SPW1 \times DE1$, $DE2 \times SPW2$) producing D0 with unknown efficiencies (Moudden & Forbes, 2008). With $s = 0$, D0 is not
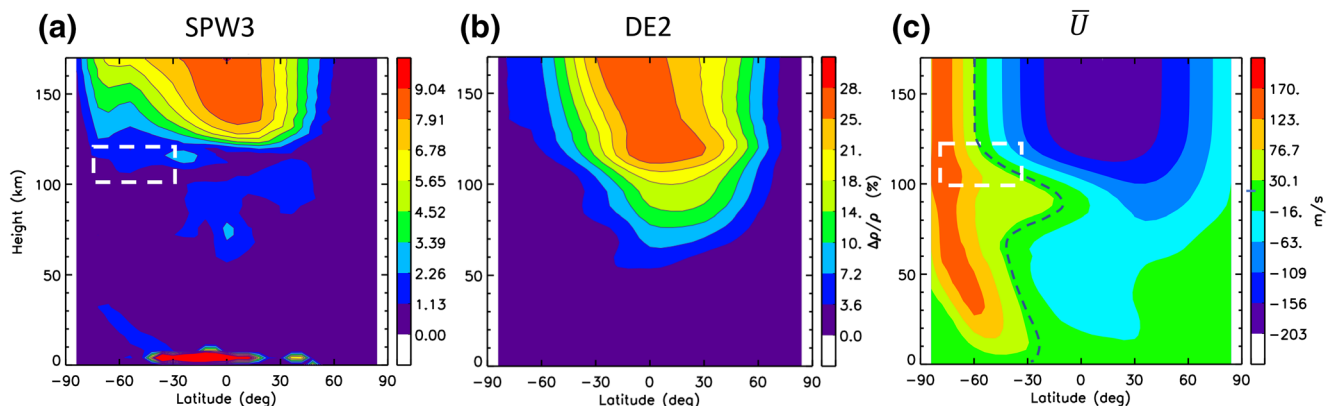

Figure 8. Same as Figures 6 and 7, except for wave-3 longitude structures in density. Note that the longitude scales only extend from 0° to 120°, since for wave-3 the structures between 120° and 240° and 240° and 360° longitude by definition duplicate those between 0° and 120°.

Table 1
Mean Values and Standard Deviations (SD) of the TGO_{2sm} and MCD_{samp_2sm} Wave-k Amplitudes in the Supporting Information

	Altitude	TGO/MCD	k	Mean (%)	SD (%)
	Periapsis	TGO	1	19.5	6.48
	Periapsis	MCD	1	9.70	5.99
	Periapsis	TGO	2	14.4	7.05
	Periapsis	MCD	2	7.92	4.81
	Periapsis	TGO	3	8.93	5.42
	Periapsis	MCD	3	5.04	3.25
	112 km	TGO	1	18.4	9.51
	112 km	MCD	1	9.60	6.21
	112 km	TGO	2	11.7	7.34
	112 km	MCD	2	6.10	3.37
	112 km	TGO	3	10.6	4.46
	112 km	MCD	3	4.73	1.55
	119 km	TGO	1	18.9	8.15
	119 km	MCD	1	9.18	4.45
	119 km	TGO	2	15.1	6.80
	119 km	MCD	2	6.19	2.80
	119 km	TGO	3	12.4	7.13
	119 km	MCD	3	6.31	1.81

Doppler-shifted by the zonal-mean wind field and also has a long vertical wavelength, and thus its accessibility to the thermosphere may not be as impacted by mean winds and dissipation as other waves. SW1 as shown in Figure 3c is likely produced by $SPW1 \times SW2$ nonlinear interaction.

In each panel of Figure 3, the dashed-white rectangles indicate the approximate $-30°$ to $-75°$ latitudinal extent, and 100–120 km extent, of the TGO density measurements. Note that within these rectangles, the range of wave-1 density perturbations from each of these sources is 0–15% for SPW1, 0–5% for D0, and 3–6%

Table 2
Values of n, s, k = |s − n|, and $dt_{LST}/d\lambda$ for Various Tides and SPWs Considered Pertinent to the Present Study

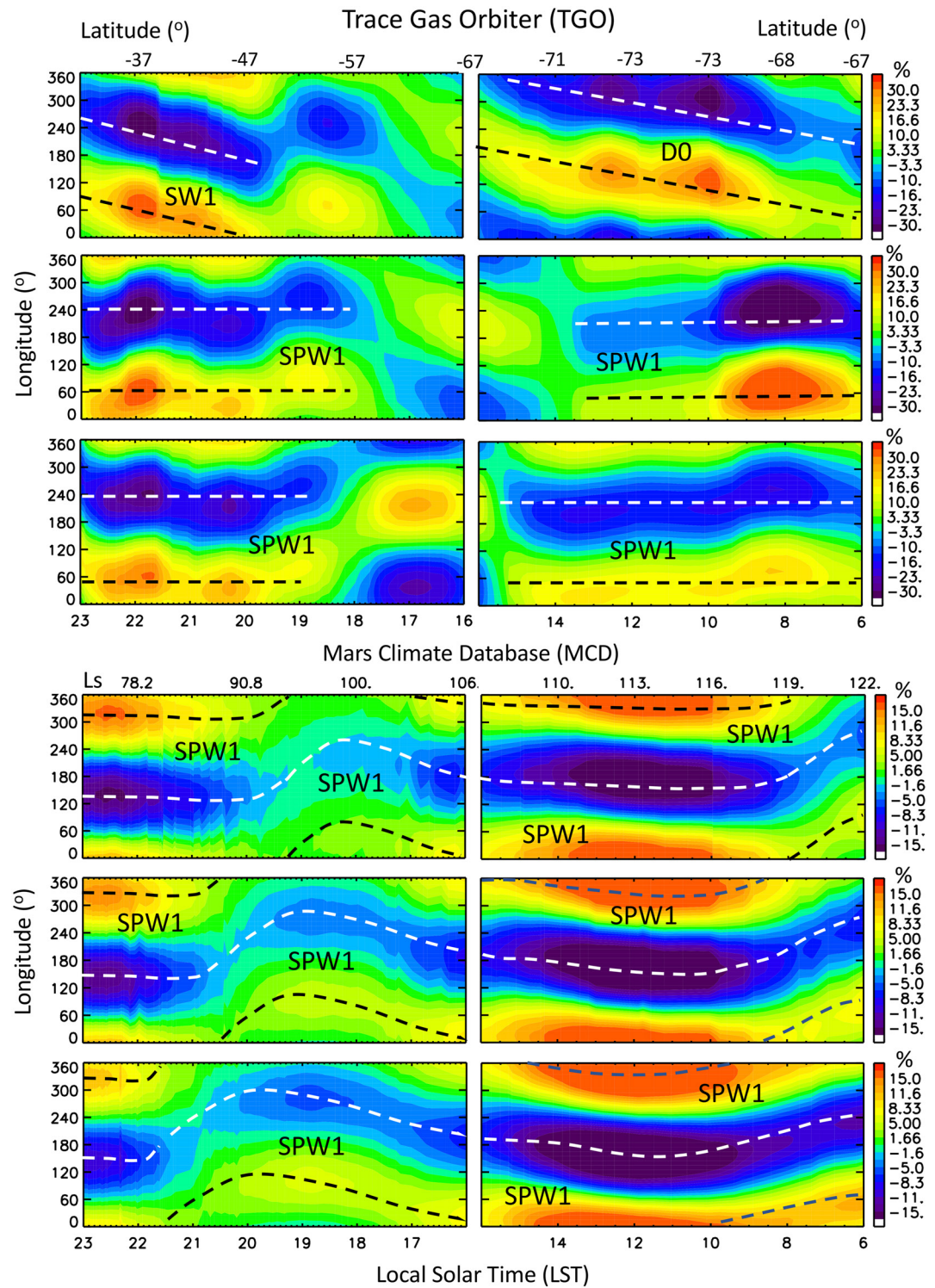|	Tide	n, s	k = |s − n|	$dt_{LST}/d\lambda$
	D0	1,0	1	+4 h/60°
	DW2	1,2	1	−4 h/60°
	SW1	2,1	1	+2 h/60°
	SPW1	0,1	1	0
	DE1	1, − 1	2	+8 h/60°
	S0	2,0	2	+4 h/60°
	TW1	3,1	2	+2.66 h/60°
	SPW2	0,2	2	0
	DE2	1, − 2	3	+12 h/60°
	SE1	2, − 1	3	+6 h/60°
	T0	3,0	3	+4 h/60°
	SPW3	0,3	3	0

Figure 3. Height-latitude structures of % density residuals from zonal mean for (a) SPW1, (b) D0, and (c) SW1, from the MCD climatological Mars month corresponding to Ls = 90–120°. All three waves give rise to $k = |s - n| = 1$ longitude structures. The dashed-white rectangle indicates the region of space containing the TGO densities analyzed in this paper. TGO, Trace Gas Orbiter.

Figure 4. Height-latitude structures of % density residuals from zonal mean for (a) SPW2 and (b) DE1, (c) DW1 and (d) S0 from the MCD climatological Mars month corresponding to Ls = 90–120°. SPW2, DE1 and S0 all give rise to $k = |s - n| = 2$ longitude structures. The dashed-white rectangle indicates the region of space containing the TGO densities analyzed in this paper. TGO, Trace Gas Orbiter; MCD, Mars Climate Database.
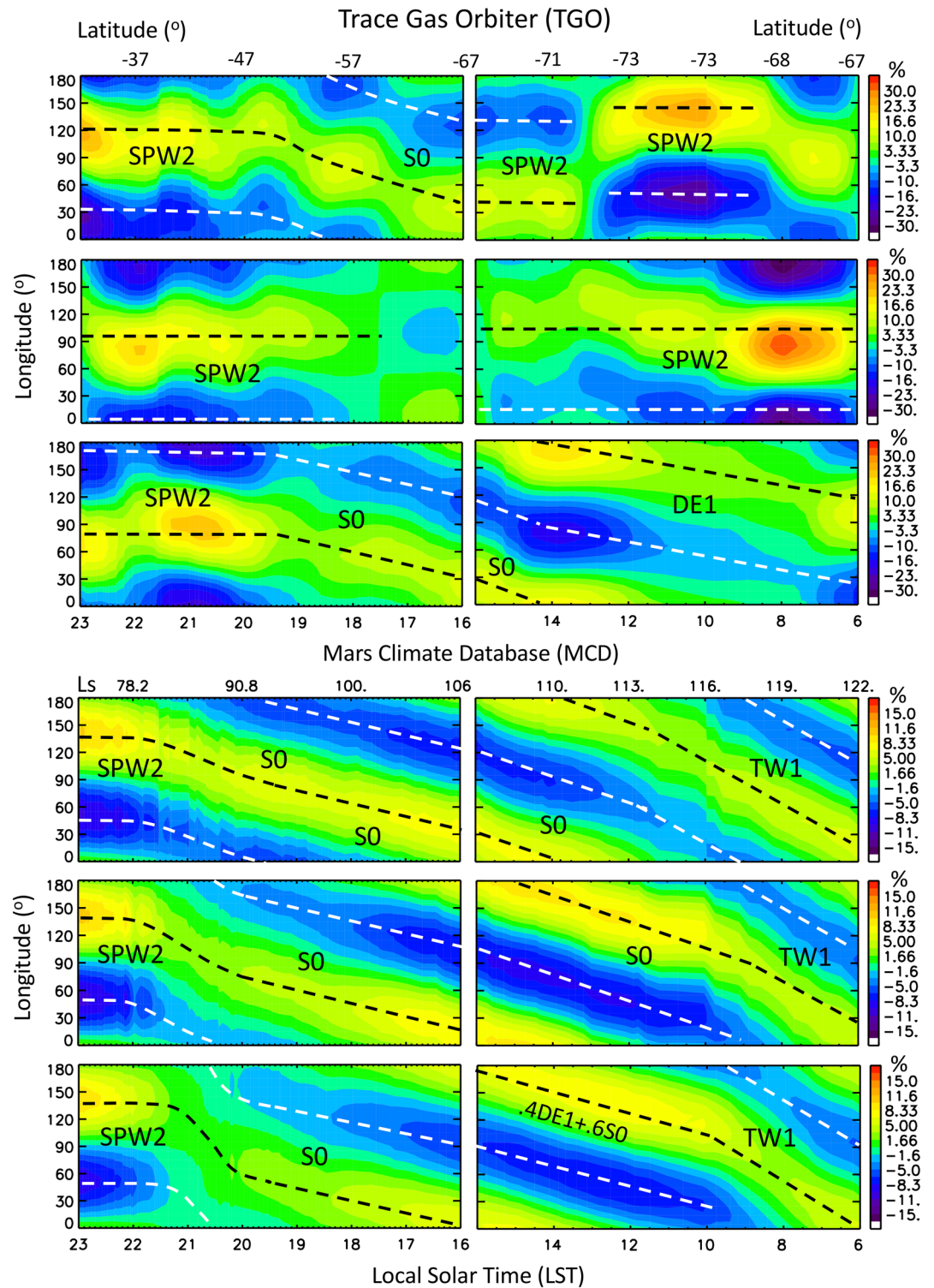
Figure 5. Height-latitude structures of % density residuals from zonal mean for (a) SPW3 and (b) DE2 from the MCD climatological Mars month corresponding to Ls = 90–120°. Both waves give rise to $k = |s − n| = 3$ longitude structures. Panel (c) displays the zonal-mean zonal wind $\bar{U}$ distribution. The dashed-white rectangle indicates the region of space containing the TGO densities analyzed in this paper. TGO, Trace Gas Orbiter; MCD, Mars Climate Database.
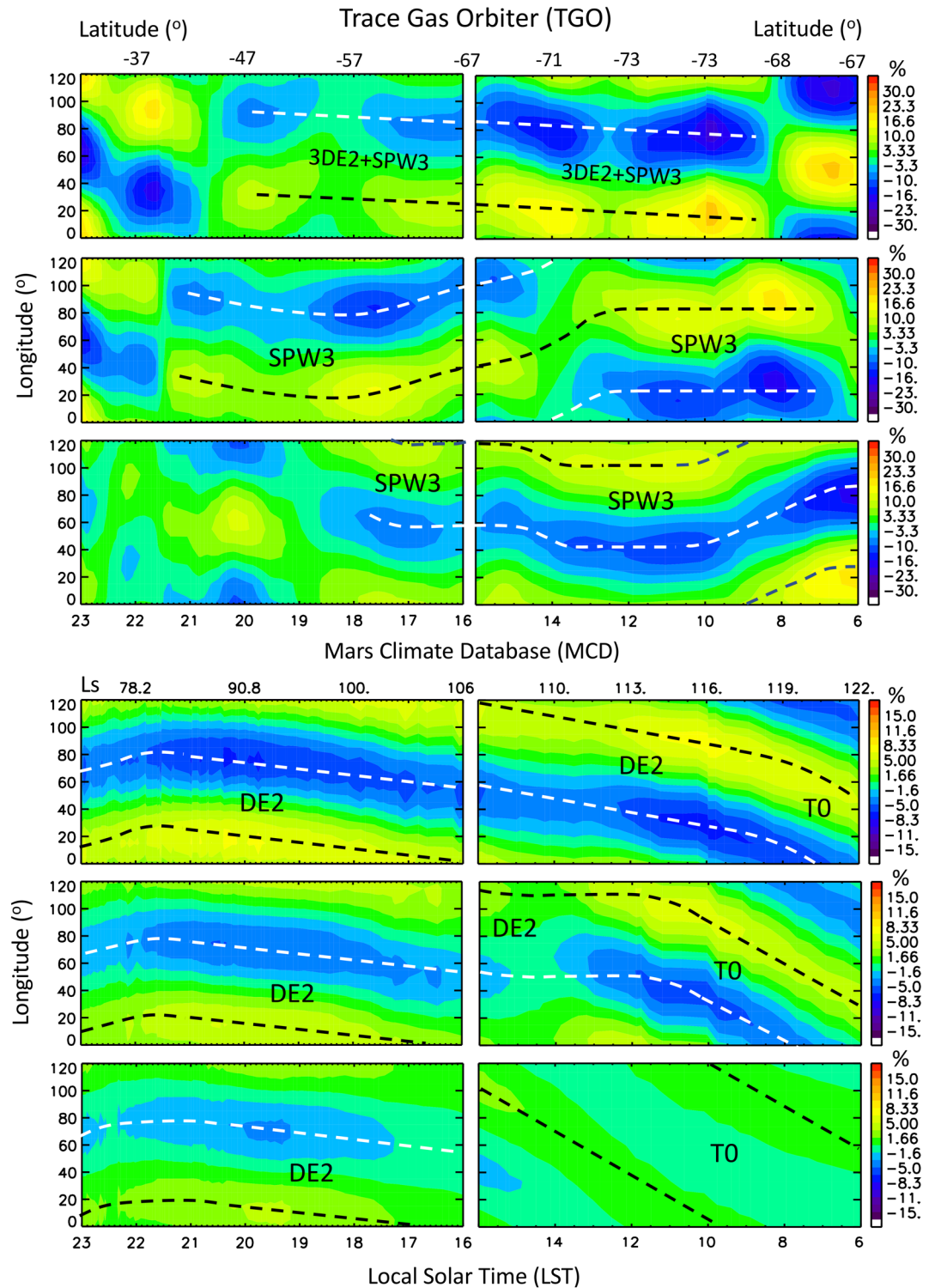
for SW1. It is worth remembering from section 2.3 that the model tends to underestimate TGO variability by about a factor of two.

Figure 4 illustrates the height-latitude structures of waves contributing most to wave-2 longitude variability in the MCD, and that also are inferred to be present in TGO data in the following section, namely SPW2, DE1, and S0. DE1 is one of the largest contributors to thermosphere density variability, achieves maximum values of about 25% at low latitudes, is broad in latitudinal extent, and undergoes significant latitude-height distortion due to the effects of mean winds (J. M. Forbes et al., 2020). The DE1 maximum near the S. pole between 100 and 120 km is interpreted by Forbes et al. (2020) as the SW− resulting from the nonlinear interaction $SPW1 \times D0$. SPW2 and S0 above 100 km as illustrated in Figures 4a and 4d in turn result as the SW− and SW+ from the $DW1 \times DE1$ nonlinear interaction, while S0 additionally results from upward propagation from the lower atmosphere (Forbes et al., 2020). Also shown in Figure 4c is the height-latitude distribution corresponding to DW1. As noted previously, DW1 is a migrating tide and is thus not seen in the TGO dataset, but it is important to study its distribution as it can originate, through wave-wave interaction, some of the components observed by TGO. DW1 amplitudes are of order 15–30% in the 100–120 km height regime. The maximum at nonpolar latitudes is due to the DW1 propagating upward from the lower atmosphere, while the large amplitudes above ∼150 km are associated with in situ solar heating. The maximum over the S. Pole above 100 km, and possibly the nearby (−30° to −60° latitude) lobe extending down to 120 km, is interpreted as the SW+ due to the same $SPW1 \times D0$ interaction noted above that produces DE1 at the S. Pole (Figure 4b). The large amplitudes of DW1 and DE1 and their global extents make possible the importance of these nonlinear interactions as global-scale sources of SPW2 and S0.

Analogous to SPW2 and DE1 in Figures 4, Figure 5 presents SPW3 and DE2. These waves will be referred to in section 3.3 in the context of interpreting wave-3 longitudinal structures in TGO density. The height-latitude structure of DE2 is not very different from DE1, and is characterized by similar broad latitude extent and large amplitudes. SPW3 results as the SW− from the $DW1 \times DE2$ nonlinear interaction. This interaction also gives rise to SW+ = SE1, which however is not relevant to data interpretations in section 3.3. Although not inferred from TGO measurements in section 3.3, one additional tide contributing to wave-3 in the high-latitude summer hemisphere according to the MCD is the zonally symmetric terdiurnal tide, T0. Due to the large thermosphere amplitudes of DE2 and SW2 during Southern Hemisphere winter (Forbes et al., 2020), it is likely that their interaction is the major source of T0: $[1, -2] \times [2, +2] \rightarrow [3, 0] + [1, +4]$. A potential secondary source is $D0 \times S0$: $[1, 0] \times [2, 0] \rightarrow [3, 0] + [1, 0]$.

Referencing again the dashed-white rectangles in Figures 3–5, another characteristic that DE1, DE2, SPW2, and SPW3 share in common is the absence of any significant amplitudes within the domain of space accessed by the TGO accelerometer. On the other hand, as noted above, they are presented here because they are relevant to interpretation of TGO densities in section 3. This disparity between the MCD and forthcoming observational results is now discussed.

Figure 5c presents the zonal-mean zonal wind ($\bar{U}$) distribution for the Ls = 90–120° MCD climatology. Forbes et al. (2020) emphasize the importance of mean wind effects on tidal propagation at Mars. At Mars, the zonal phase speed ($C_{ph} = -n\Omega \cos\theta/s$, θ = latitude) of DE1(DE2) is 241(121)$\cos\theta$m s^{-1}, as compared with 463(232) $\cos\theta$m s^{-1} at Earth, mainly due to differences in the radii of the planets (6,370 km for Earth; 3,397 km for Mars). These combine with the large values of $\bar{U}$ at Mars (∼±175 m s^{-1}, refer to Figure 5c), which are roughly twice those at Earth over a similar altitude regime (Drob et al., 2015), to make tidal propagation at Mars particularly susceptible to the $\bar{U}$ distribution. In the present context, this is particularly exacerbated at high southern latitudes where $\cos\theta \leq 0.5$ (i.e., poleward of −60°); it is here where critical levels $C_{ph} = \bar{U}$ can occur. Put simply, eastward-propagating tides tend to avoid propagation into eastward ($\bar{U} > 0$) mean wind regimes, where Doppler-shifting to lower frequencies with attendant shorter vertical wavelengths result in enhanced dissipation (see discussion of these effects in the context of solar-asynchronous tidal propagation at Earth in Ekanayake et al., 1997). The same can be said for westward-propagating waves in terms of avoiding westward ($\bar{U} < 0$) mean wind regimes. By the same token, eastward-(westward-) propagating waves favor propagation in westward(eastward) mean wind regimes where critical levels are absent and Doppler-shifting to higher frequencies occurs. In this context we note the intrusion of the winter jet into low S. Hemisphere latitudes around 90 km altitude illustrated in Figure 5c. DE2 (Figure 5b) avoids this eastward wind intrusion, resulting in the DE2 maximum below 100 km being shifted into the N.

Hemisphere. This intrusion also appears to be connected with the bite-out in the DE1 amplitude structure between 80 and 120 km and −30° to −60° latitude in Figure 4b.

In addition to Doppler-shifting, the meridional shear of $\bar{U}$, which is quite significant in the S. Hemisphere polar region (cf. Figure 5c), can also affect tidal propagation (McLandress, 2002; Takahashi et al., 2006). However, it is more difficult to heuristically diagnose these influences without supplementary modeling.

There are few observational constraints on the $\bar{U}$ distribution in Mars atmosphere, which is model dependent, and thus open to considerable uncertainty. For instance, compare Figure 5c with Figure 8 in Forget et al. (1999), which shows that the same model, but with a different dynamical core, predicts a much different winter zonal jet (whereas everything else remains the same). Gravity waves likely play a role in determining $\bar{U}$ at Mars (Forget et al., 1999; Gilli et al., 2020; Medvedev et al., 2011). Recent LMD model results that include a nonorographic gravity wave parameterization (Gilli et al., 2020) in fact yield a winter hemispheric jet at Ls = 90–120° that is considerably reduced in magnitude above about 80 km as compared with Figure 5c, and yield much-reduced westward winds above 100 km at low latitudes as compared with Figure 5c. Based upon the above Doppler-shifting arguments, both of these $\bar{U}$ changes would likely impact the latitude structures of DE1 and DE2 contained in Figures 4b and 5b. In particular, a less prominent high-latitude winter jet would no longer preclude expansion of these tidal structures into the region of space sampled by the TGO accelerometer. SPW2 and SPW3 would also be affected, since they are generated through nonlinear interaction between DE1 and DE2, respectively, and DW1. We will return to these points later in the course of interpreting the TGO longitudinal structures.

3. Results

3.1. Wave-1 Longitude Structures

Figure 6 focuses on wave-1 longitude structures in TGO densities (top six panels) with complementary information from MCD (bottom six panels), all plotted versus LST in order to apply equation (6). The left-column of panels in Figure 6 all correspond to the nonpolar phase indicated in Figure 1a, and the right column of panels correspond to the polar phase indicated in Figure 1a. For each set of TGO and MCD panels, the bottom row corresponds to periapsis altitudes, the middle row to 112 km, and the top row to 119 km. As noted in section 2, the MCD results are formed through interpolation of MCD climatological files corresponding to "Mars months" Ls = 30–60°, Ls = 60–90°, Ls = 90–120°, and Ls = 120–150°. Smooth transitions of the longitude structures from one Mars month to the next in the MCD panels can be seen around Ls = 90° and Ls = 120°. Interpretations (i.e., dashed lines drawn to connect one wave structure to another) in terms of phase transitions and discontinuities are double-checked against figures similar to Figure 2i and included in the Supplementary Information, which provide a somewhat broader perspective on phase trends as a function of Ls. Figures 7 and 8 are similar presentations for the wave-2 and wave-3 longitude structures.

In Figure 6, the MCD indicates that the main contributor to the wave-1 structure is SPW1 during both nonpolar and polar phases. SPW1 is a common feature of the winter polar lower and middle atmosphere of Mars. As shown in Forbes et al. (2020), in the MCD SPW1 originates below 100 km altitude, extends between Ls = 30–180° and 30–170 km altitude from about −30° latitude to the vicinity of the S. Pole, and achieves maximum amplitudes near 75–80° of order 20% near 100 km. MCD SPW1 phases are nearly independent of altitude. The MCD SPW1 undergoes a phase transition in time and/or latitude between Ls = 85° and 105°, ultimately approaching a phase (longitude of maximum, λ_{max}) around $\lambda_{max} \sim 180°$, not too different from its $\lambda_{max} \sim 150$–180° phase near the pole around Ls = 106–120°. Amplitudes range between about 5% and 15% through the nonpolar and polar phases, with the higher amplitudes occurring near the pole in agreement with the behavior shown in Figure 3a.

In many respects, the TGO wave-1 behavior depicted in the top panels of Figure 6 is not too different from MCD, except amplitudes are about a factor of two larger. At periapsis and 112 km, near-constant phase and amplitude with time and/or latitude during the nonpolar phase suggests dominance of SPW1, followed by a transition between Ls = 100–110° to SPW1 once again with similar phase in the polar region compared to the nonpolar phase. There is little phase change with height throughout the nonpolar phase. At 119 km in the polar phase (top right panel in Figure 6), the phase tilt is close to 4 h/60°, consistent with a D0 interpretation (refer to Table 2). At 119 km in the nonpolar phase (top left panel in Figure 6), the longitude structure

is similar to that at lower altitudes, but with some distortion and downward (westward in longitude and decreasing with LST) phase tilt; prior to Ls = 90° this phase tilt is consistent with SW1 (2 h/60°, Table 2), twice as steep as D0 (note that LSTs span 7 h in the nonpolar phase, and 10 h in the polar phase, so the same slopes appear differently in the two phases). There are sharp transitions in phase between Ls = 90° and Ls = 110° that prevent any interpretation in terms of tidal or SPW origins of the wave-1 structures in TGO. This is apparently just part of the disturbed dynamics that characterizes this region of Mars' atmosphere.

The periapsis of MRO during aerobraking traversed the S. Polar region around Ls = 70–85°, and descended in latitude to −20° by Ls ∼100°, i.e., also around winter solstice. Using an analysis also centered around expression (6), Forbes and Zhang (2018) interpreted the wave-1 density structures in the polar region in terms of SPW1 and D0, and similarly for MO aerobraking densities during N. Hemisphere winter. These waves appear to be a regular feature of the winter polar regions in Mars lower thermosphere. D0 and SW1 do exist at these altitudes and poleward of −30° latitude in the MCD (see Figure 3b), and could combine with SPW1 to produce the general downward tilt of the MCD phase structures in Figure 6 between Ls = 90° and 120°, and moreover support the plausibility of D0 and SW1 interpretations in the TGO data at 119 km in Figure 6.

3.2. Wave-2 Longitude Structures

The wave-2 structures in TGO and MCD are displayed in Figure 7, in identical format as Figure 6. Note that the longitude scales in Figure 7 only extend from 0° to 180°, since for wave-2 the structures between 180° and 360° longitude by definition duplicate those between 0° and 180°. In the nonpolar phase, at all three altitudes MCD is dominated by SPW2 prior to Ls = 90°, and by S0 thereafter. In the initial part of the polar phase, the structures are consistent with some combination of DE1 and S0, transitioning to TW1 thereafter. The MCD wave-2 amplitudes are modest, less than ±10%. As noted in section 2, SPW2 and S0 arise as secondary waves from the $DW1 \times DE1$ interaction, so the amplitudes and height-latitude structures of SPW2 and S0 are tied to those of DE1. Moreover, DE1 is in turn dependent on the zonal-mean zonal wind ($\bar{U}$) distribution, which is open to considerable uncertainty.

As mentioned in section 2, there is modeling evidence that the intensity and vertical extent of the polar winter eastward jet is overestimated in the MCD, and if this is true, then DE1 could extend significantly more poleward at the altitudes of TGO than in the MCD, and thereby modify SPW2 and S0, but in less predictable manners. TW1 was not mentioned in section 2 since it does not appear relevant to the interpretation of TGO. TW1 can arise as the SW + resulting from the $DW1 \times S0$ nonlinear interaction.

The TGO wave-2 structures in Figure 7 also contain signatures of SPW2, S0, and DE1, but with SPW2 playing a more prominent role than in the MCD. Except for the indications of S0 or DE1 presence in the top six panels of Figure 7, there is no other evidence of sustained phase tilt that can readily be interpreted in the context of expression (6) and Table 2. The wave-2 amplitudes attributed to SPW2 are nearly constant with time, with some oscillatory features superimposed, or with an occasional phase jump (i.e., as illustrated at 119 km around Ls = 112° in the top right panel of Figure 7). The reader may also find it helpful to view the wave-2 phase plots in Figures S3–S5 in the supporting information for a somewhat alternative perspective on why such extensive attribution to SPW2 appears to be the only logical choice.

The fact that the SPW2 amplitude structure in the polar region lies over that of DE1 near the pole, is consistent with the MCD depictions in Figures 4a and 4b, except that the MCD SPW2 amplitude maximum does not quite extend down far enough into the region of space accessed by the TGO accelerometer. In the same vein, while SPW2 and DE1 amplitudes are strong between 100 and 120 km at low latitudes in the MCD, they do not quite extend poleward enough to play an important role in the MCD wave-2 structures in Figure 7. Consistent with the theme of previous arguments, it seems that this can be traced to an overextension of the eastward winter polar jet to altitudes above about 80 km in the MCD.

3.3. Wave-3 Longitude Structures

The longitudinal wave structures for MCD and TGO are illustrated in Figure 8. With the same reasoning noted in connection with Figure 7, the longitude scales in Figure 8 only extend from 0° to 120°. The MCD

is dominated by DE2 in the nonpolar phase, and transitions to T0 in the polar phase. The DE2 amplitudes increase with height between periapsis and 120 km, consistent with Figure 5b. Note that DE2 amplitudes between Ls = 90° and 100° are influenced (through the interpolation scheme) to some degree by the Ls = 60–90° and Ls = 120–150° MCD climatologies. The DE2 amplitudes at these latitudes are fairly small (~±6%) compared to the >25% maximum at low latitudes, and are likely diminished locally at TGO heights and latitudes by the mean wind effect described previously. T0 was not mentioned in section 2, since it does not appear in the TGO densities. It can be generated as the SW+ of the nonlinear interaction $D0 \times S0$, and has a phase tilt distinctly steeper than DE2.

As indicated in the top panels of Figure 8, SPW3 appears to be the dominant contributor to wave-3 longitudinal structures in TGO, with some influence of DE2 at 119 km. In that case, a linear combination consisting of three parts DE2 and one part SPW3 fit well, and is consistent with the importance of DE2 as delineated in the MCD (Figure 5b). Wave-3 underwent some phase disruption at all altitudes between about Ls = 75° and 90°, making it difficult to apply expression (6). During other times, there are basically no good matches to the phase progressions listed in Table 2, except the connected with a stationary wave (0 h/60°). As noted in section 2, and following the logic put forth in connection with wave-2, our interpretation is that DE2 is inhibited from entering the spatial domain where the TGO accelerometer measurements originate by the intense eastward jet that exists at high latitudes in the MCD (Figure 5c). This in turn affects the distribution of SPW3, which arises from the $DW1 \times DE2$ nonlinear interaction. The appearance of SPW3 in the TGO data suggests that this nonlinear interaction is not emulated well in the MCD, at least not in the S. Hemisphere at 100–120 km altitude.

4. Summary and Conclusions

This paper is devoted to delineating and interpreting the longitudinal structures in thermosphere densities measured by the accelerometer on the ExoMars TGO Mission. The specific data analyzed are the percent residuals from zonal-mean densities at periapsis (102–109 km), 112 km, and 119 km, as periapsis migrated from −30° to −72° latitude between Ls = 70° and 105°, and then to −65° by Ls = 122°. During this time, wave-1, wave-2, and wave-3 longitudinal structures were extracted within moving windows of linearly decreasing length of 35 to 5 sols, accommodated by the increasingly improved longitude coverage as the satellite orbit contracted with time. Coincidentally, the local solar time (LST) decreased from 22:00 to 16:00 h during the "nonpolar" phase (equatorward of −65° latitude), and from 16:00 to 06:00 h during the "polar" phase.

Interpolations between Ls = 60° and 90°, Ls = 90° and 120°, and Ls = 120° and 150° Mars Climate Database (MCD) climatologies were used to provide a physical basis for scientific interpretation, and also to assess the influence of satellite sampling on the extracted longitudinal structures. Concerning the latter, MCD densities were sampled in space and time (height, latitude, longitude, UT, and LST) identically to how the TGO accelerometer sampled Mars' thermosphere, and wave-1, wave-2, and wave-3 longitudinal structures were extracted following the same procedure as applied to TGO. By comparing these structures with those extracted from the MCD with full longitudinal coverage, it was discovered that the sampling introduced a temporal variability of its own when displayed as window-mean amplitudes and phases moving forward one sol at a time. A suitable smoothing algorithm was applied to the TGO densities to mitigate this effect, after first testing against the TGO-sampled MCD results to ensure that the integrity of the TGO longitudinal structures and their evolutions with respect to longitude and LST were not compromised.

The wave origins of the TGO longitudinal density structures were deduced by matching their phase progressions with respect to longitude and LST with those constrained mathematically based on the periods and zonal wavenumbers of candidate waves suggested on a physical basis by the MCD and discussed in detail by Forbes et al. (2020). Results and conclusions to emerge from this analysis are as follows:

1. When cast relative to the zonal mean, thermosphere density perturbations in the MCD due to upward-propagating tides do not reflect any significant differences when compared between average and minimum conditions (i.e., E10.7 = 140 as in Forbes et al. (2020), vs. E10.7 = 80 as in the present study).

Although confirming what might be expected intuitively, this is an important point to keep in mind when making model-data or data-data comparisons of this type between different levels of solar activity

2. The wave-1 TGO density structures primarily originate from SPW1 at both nonpolar latitudes and polar latitudes at altitudes ≤112 km. At 119 km, SW1 captures much of the variability at nonpolar latitudes, while D0 captures all of the variability at polar latitudes. In the MCD, the primary contributor to wave-1 density variability at both polar and nonpolar latitudes is SPW1 at all three TGO altitudes

3. For wave-2, SPW2 explains most of the TGO variability equatorward of $-40°$ to $-50°$ latitude during the nonpolar phase at all three altitudes, and at polar latitudes at 119 km altitude. Between about $-50°$ and $-65°$, wave-2 in TGO appears to originate from S0 at periapsis and 119 km, but is indeterminable at 112 km. In the nonpolar phase, MCD also shows wave-2 to transition from an SPW2 to S0 origin, although the transition occurs somewhat earlier (Ls ∼85°, $-40°$ latitude). In the polar phase, SPW2 is not among the waves contributing to wave-2 in the MCD; instead, S0, DE1, and TW1 are the contributing waves. However, significant SPW2 amplitudes do exist in the MCD in close proximity to the region of space accessed by the TGO accelerometer

4. The origins of wave-3 in TGO densities are indeterminable equatorward of about $-40°$ to $-50°$ latitude, depending on altitude. Otherwise, the main contributor to wave-3 TGO density structures is SPW3, with some evidence of the presence of DE2 at 119 km at both polar and nonpolar latitudes. In the MCD, wave-3 is explained by DE2 at nonpolar latitudes and by DE2 and T0 at polar latitudes. However, significant SPW3 amplitudes do exist in the MCD in close proximity to the region space accessed by the TGO accelerometer

5. On average, for both nonpolar and polar latitudes, and for the three altitudes compared with TGO, the MCD wave-1, wave-2, and wave-3 amplitudes are about half those determined from TGO. This may be due in part to the fact that the MCD climatologies are essentially grid-point averages of hourly GCM outputs over spans of 30° Ls, which essentially yield vector-average tides. Any sol-to-sol variability in the amplitudes and phases of various wave components cited above would suffer some degree of phase cancellation and amplitude suppression as compared with amplitude averages. Another reason for the lower-amplitude wave structures in the MCD as compared with TGO may be the very distinct seasonal-latitudinal regime accessed by the TGO accelerometer; specifically, its proximity to the intense eastward polar winter jet which protrudes well into the thermosphere in the MCD (cf. Figure 5c)

It is an interesting outcome of this work that SPW2 and SPW3 emerged as primary contributors to TGO wave-2 and wave-3 density variability, respectively. SPWs are not usually associated with thermosphere dynamics at Earth or Mars. However, given that they can arise as the result of interactions between the three largest (≳ 25%) global-scale tidal components in the Martian thermosphere (DW1, DE1, DE2), it is perhaps not surprising that they exist at significant amplitudes. Indeed, they also exist in the MCD at similar amplitudes to TGO in close proximity to the height-latitude region where the TGO measurements were made. A further relevant point is that eastward-propagating waves tend not to propagate into strong prevailing eastward wind regimes. It is our interpretation that in the current version of the MCD, the winter polar jet blocks poleward expansion of DE1 and DE2 beyond $-30°$ latitude, precluding their intrusion into the space regime accessed by the TGO accelerometer. This restriction on DE1 and DE2 undoubtedly impacts the structures of SPW2, S0 and SPW3 that arise from in situ nonlinear interaction between DE1 and DE2, respectively, with the diurnal migrating tide (DW1).

The above reasoning is consistent with recent LMD GCM simulations that include a nonorographic gravity wave parameterization (Gilli et al., 2020), and in fact yield a winter hemispheric jet at Ls = 90–120° that is considerably reduced in magnitude above about 80 km as compared with Figure 5c. The TGO results presented here, as well as aerobraking data from MGS, MO, and MRO, and extensive information on longitudinal structures in density from MAVEN, will help pave the way for a future MCD release that includes improved physics and that is validated against thermospheric density observations. Such an advance would certainly move us an important step forward with regard to understanding and predicting aerobraking-region density variability.

References

Angelats i Coll, M., Forget, F., Lòpez-Valverde, M. A., Read, P. L., & Lewis, S. R. (2004). Upper atmosphere of Mars up to 120 km: Mars Global Surveyor accelerometer data analysis with the LMD general circulation model. *Journal of Geophysical Research*, *109*, E01011. https://doi.org/10.1029/2003JE002163

Drob, D. P., Emmert, J. T., Meriwether, J. W., Makela, J. J., Doornbos, E., Conde, M., et al. (2015). An update to the Horizontal Wind Model (HWM): The quiet time thermosphere. *Earth and Space Science*, *2*, 301–319. https://doi.org/10.1002/2014EA000089

Ekanayake, E. M. P., Aso, T., & Miyahara, S. (1997). Background wind effect on propagation of nonmigrating diurnal tides in the middle atmosphere. *Journal of Atmospheric and Solar-Terrestrial Physics*, *59*, 401–429.

England, S. L., Liu, G., Kumar, A., Mahaffy, P. R., Elrod, M., Benna, M., et al. (2019). Atmospheric tides at high latitudes in the Martian upper atmosphere observed by MAVEN and MRO. *Journal of Geophysical Research: Space Physics*, *124*, 2943–2953. https://doi.org/10.1029/2019JA026601

England, S. L., Liu, G., Withers, P., Yiğit, E., Lo, D., Jain, S., et al. (2016). Simultaneous observations of atmospheric tides from combined in situ and remote observations at Mars from the MAVEN spacecraft. *Journal of Geophysical Research: Planets*, *121*, 594–607. https://doi.org/10.1002/2016JE004997

Forbes, J. M., Bridger, A. F. C., Bougher, S. W., Hagan, M. E., Hollingsworth, J. L., Keating, J. M., & Murphy, J. (2002). Nonmigrating tides in the thermosphere of Mars. *Journal of Geophysical Research*, *107*(E11), 5113. https://doi.org/10.1029/2001JE001582

Forbes, J. M., & Hagan, M. E. (2000). Diurnal Kelvin wave in the atmosphere of Mars: Toward an understanding of "stationary" density structures observed by the MGS accelerometer. *Geophysical Research Letters*, *27*, 3563–3566.

Forbes, J. M., & Zhang, X. (2018). Polar region variability in the lower thermosphere of Mars from Odyssey and Reconnaissance Orbiter aerobraking measurements. *Journal of Geophysical Research: Space Physics*, *123*, 8664–8687 https://doi.org/10.1029/2018JA025527

Forbes, J. M., Zhang, X., Angelats i Coll, M., & Keating, G. M. (2004). Nonmigrating tides in the thermosphere of Mars: A quasi-empirical description. *Advances in Space Research*, *34*, 1690–1695.

Forbes, J. M., Zhang, X., Forget, F., Millour, E., & Kleinböhl, A. (2020). Solar tides in the middle and upper atmosphere of Mars. *Journal of Geophysical Research: Space Physics*, *125*, e2020JA028140. https://doi.org/10.1029/2020JA028140

Forget, F., Hourdin, F., Fournier, R., Hourdin, C., Talagrand, O., Collins, M., et al. (1999). Improved general circulation models of the Martian atmosphere from the surface to above 80 km. *Journal of Geophysical Research*, *104*, 24155–24175

Forget, F., Montmessin, F., Bertaux, J.-L., González-Galindo, F., Lebonnois, S., Quémerais, E., et al. (2009). Density and temperatures of the upper Martian atmosphere measured by stellar occultations with Mars Express SPICAM. *Journal of Geophysical Research*, *114*, E01004. https://doi.org/10.1029/2008JE003086

Gilli, G., Forget, F., Spiga, A., Navarro, T., Millour, E., Montabone, L., et al. (2020). Impact of gravity waves on the middle atmosphere of Mars: A non-orographic gravity wave parameterization based on global climate modeling and MCS observations. *Journal of Geophysical Research*, *125*, e2018JE005873. https://doi.org/10.1029/2018JE005873

González-Galindo, F., Chaufray, J.-Y., López-Valverde, M. A., Gilli, G., Forget, F., Leblanc, F., et al. (2013). Three-dimensional Martian ionosphere model: I. The photochemical ionosphere below 180 km. *Journal of Geophysical Research: Planets*, *118*, 2105–2123. https://doi.org/10.1002/jgre.20150

González-Galindo, F., Forget, F., Lápez-Valverde, M. A., Angelats i Coll, M., & Millour, E. (2009). A ground-to-exosphere Martian general circulation model: 1. Seasonal, diurnal, and solar cycle variation of thermospheric temperatures. *Journal of Geophysical Research*, *114*, E04001. https://doi.org/10.1029/2008JE003246

González-Galindo, F., López-Valverde, M. A., Forget, F., Garciá-Comas, M., Millour, E., & Montabone, L. (2015). Variability of the Martian thermosphere during eight Martian years as simulated by a ground-to-exosphere global circulation model. *Journal of Geophysical Research: Planets*, *120*, 2020–2035. https://doi.org/10.1002/2015JE004925

Joshi, M. M., Hollingsworth, J. L., Haberle, R. M., & Bridger, A. F. C. (2000). An interpretation of Martian thermospheric waves based on analysis of a general circulation model. *Geophysical Research Letters*, *27*, 613–616.

Justh, H. L., & Justus, C. G. (2007). Mars Global Reference Atmospheric Model (Mars-GRAM 2005) applications for mars science laboratory mission site selection processes. In *7th International Conference on Mars*, Pasadena, CA, USA, July 09-13, 2007, . Retrieved from https://ntrs.nasa.gov/search.jsp?R=20090028811

Kleinböhl, A., Schofield, J. T., Kass, D. M., Abdou, W. A., Backus, C. R., Sen, B., et al. (2009). Mars Climate Sounder limb profile retrieval of atmospheric temperature, pressure, dust and water ice opacity. *Journal of Geophysical Research*, *114*, E10006. https://doi.org/10.1029/2009JE003358

Liu, G., England, S., Lillis, R. J., Mahaffy, P. R., Elrod, M., Benna, M., & Jakosky, B. (2017). Longitudinal structures in Mars' upper atmosphere as observed by MAVEN/NGIMS. *Journal of Geophysical Research: Space Physics*, *122*, 1258–1268. https://doi.org/10.1002/2016JA023455

Lo, D. Y., Yelle, R. V., Schneider, N. M., Jain, S. K., Stewart, A. I. F., England, S. L., et al. (2015). Non-migrating tides in the Martian atmosphere as observed by MAVEN IUVS. *Geophysical Research Letters*, *42*, 9057–9063. https://doi.org/10.1002/2015GL066268

McLandress, C. (2002). The seasonal variation of the propagating diurnal tide in the mesosphere and lower thermosphere: Part II. The role of tidal heating and zonal mean wind. *Journal of the Atmospheric Sciences*, *59*, 907–922.

Medvedev, A. S., Yiğit, E., Hartogh, P., & Becker, E. (2011). Influence of gravity waves on the Martian atmosphere: General circulation modeling. *Journal of Geophysical Research*, *116*, E10004. https://doi.org/10.1029/2011JE003848

Millour, E., Forget, F., et al. (2018). *The Mars climate database (version 5.3). Scientific Workshop: From Mars express to ExoMars*, 27–28 February 2018. Madrid, Spain: ESAC.

Montabone, L., Spiga, A., Kass, D. M., Kleinboehl, A., Forget, F., & Millour, E. (2020). Martian year 34 column dust climatology from mars climate sounder observations: Reconstructed maps and model simulations. *Journal of Geophysical Research: Planets*, *125*, e2019JE006111. https://doi.org/10.1029/2019JE006111

Montmessin, F., Korablev, O., Lefèvre, F., Bertaux, J.-L., Fedorova, A., Trokhimovskiy, A., et al. (2017). SPICAM on Mars Express: A 10 year in-depth survey of the Martian atmosphere. *Icarus*, *297*, 195–216. https://doi.org/10.1016/j.icarus.2017.06.022

Moudden, Y., & Forbes, J. M. (2015). Density prediction in Mars' aerobraking region. *Space Weather*, *13*, 86–96. https://doi.org/10.1002/2014SW001121

Moudden, Y., Forbes, J. M., Spiga, A., Vals, M., Zakharov, V., Montabone, L., et al. (2008). Topographic connections with density waves in Mars' aerobraking regime. *Journal of Geophysical Research*, *113*, E11009. https://doi.org/10.1029/2008JE003107

Schneider, N. M., Milby, Z., Jain, S. K., González-Galindo, F., Royer, E., Gèrard, J.-C., et al. (2020). Imaging of Martian circulation patterns and atmospheric tides Through MAVEN/IUVS nightglow observations. *Journal of Geophysical Research: Space Physics*, *125*, e2019JA027318. https://doi.org/10.1029/2019JA027318

Sentman, L. H. (1961). *Free molecule flow theory and its application to the determination of aerodynamic forces*. (Tech. Rep. LMSC-448514, pp. 265–409). Sunnyvale, CA: Lockheed Missile and Space Co.

Siddle, A. G., Mueller-Wodarg, I. C. F., Bruinsma, S., & Marty, J.-C. (2020). Density structures in the Martian lower thermosphere as inferred by Trace Gas Orbiter accelerometer measurements. *Icarus*, *357*, 1–10. https://doi.org/10.1016/j.icarus.2020.114109

Takahashi, Y. O., Fujiwara, J., & Fukunishi, H. (2006). Vertical and latitudinal structure of the migrating diurnal tide in the Martian atmosphere: Numerical investigations. *Journal of Geophysical Research*, *111*, E01003. https://doi.org/10.1029/2005JE002543

Tolson, R. H., Dwyer, A. M., Hanna, J. L., Keating, G. M., George, B. E., Escalera, P. E., & Werner, M. R. (2005). Application of accelerometer data to Mars Odyssey aerobraking and atmospheric modeling. *Journal of Spacecraft and Rockets*, *42*, 435–443.

Wang, L., Fritts, D. C., & Tolson, R. H. (2006). Nonmigrating tides inferred from the Mars Odyssey and Mars Global Surveyor aerobraking data. *Geophysical Research Letters*, *33*, L23201. https://doi.org/10.1029/2006GL027753

Wilson, R. J. (2002). Evidence for nonmigrating thermal tides in the Mars upper atmosphere from the Mars Global Surveyor Accelerometer Experiment. *Geophysical Research Letters*, *29*(7), 1120. https://doi.org/10.1029/2001GL013975

Withers, P. G. (2006). Mars Global Surveyor and Mars Odyssey Accelerometer observations of the Martian upper atmosphere during aerobraking. *Geophysical Research Letters*, *33*, L02201. https://doi.org/10.1029/2005GL024447

Withers, P. G., Bougher, S. W., & Keating, G. M. (2003). The effects of topographically controlled thermal tides in the Martian upper atmosphere as seen by the MGS Accelerometer. *Icarus*, *164*, 14–32.